Sensors and Actuators A 172 (2011) 483–490

Contents lists available at SciVerse ScienceDirect

Sensors and Actuators A: Physical

journal homepage: www.elsevier.com/locate/sna

Control of ignition delay in microfabricated hot-wire igniters: Simulation, fabrication, and experimental results

Brian A. English*, Mark G. Allen

Georgia Institute of Technology, United States

ARTICLE INFO

Article history:
Received 6 February 2009
Received in revised form 7 September 2011
Accepted 9 September 2011
Available online 24 September 2011

Keywords:
Microthrusters
Igniters
Lamination-based fabrication
Microcombustors
Gas generator actuators

ABSTRACT

The presented work studied thermal interactions between laminated, metal-foil, hot-wire igniters and exothermic solid-state, composite chemical systems in order to demonstrate precise timing control of a thermal ignition process. The study includes FEA modeling, device fabrication, and characterization to demonstrate control microthruster ignition delays to within 2 ms. The modeling included studies of total ignition delay as well as the ignition delay variation versus process variations. Microthrusters were then fabricated via printed circuit board lamination, and the ignition performance was characterized. The characterization showed agreement with modeling to within 2-sigma for most cases. And the characterization demonstrated that the ignition delay could be controlled to within 0.36 and 0.84 ms for the best case. Furthermore, this performance was demonstrated with a small battery supply (200–600 mAh) and minimal electronics in the ignition system. This work extends the use of current microthrusters to short-lifetime applications that need high forces delivered in millisecond time intervals.

1. Introduction

Microthrusters are sub-cm scale devices that generate high-kinetic-energy exhausts to cause precise momentum impulses. Several devices have been developed in previous efforts using solid propellant [1–4], liquid propellant [1], electrostatic [2], or cold gas [3], among others. These are typically used for position control, such as station keeping, attitude control, and maneuvering of microsatellites [4–6], or for maneuvering of micro unmanned aerial vehicles and "Smart Dust" sensors [7]. In these applications, microthrusters are advantageous because they have a high specific impulse (impulse per unit weight) compared to traditional MEMS actuators. This is extremely important in flight vehicles where weight and volume are restricted. In addition, the various approaches enable fine tuning of the impulse profile with time, e.g., large forces over short durations or vice versa. This allows microthrusters to be tailored to specific applications and flight movements. Precise impulse, low weight, and low volume make microthrusters an attractive actuator technology as air and space vehicles become smaller and smaller.

The mission duration, size, and stabilization of the flight vehicle often determine which microthruster technology is most suitable. For example, the mission duration sets the lower limit on the amount of impulse that must be carried on the vehicle. Long mission durations favor high specific impulse microthrusters, such as electrostatic. Simple microthrusters, such as solid propellant, are more practical in small vehicles where added volume of support systems is not available. Finally, stabilization of the vehicle is important because it determines the impulse control vs. time, favoring microthrusters that can be stopped and restarted.

To show how vehicle stabilization influences actuator timing, Fig. 1 illustrates three stabilization techniques – fin, internal gyro, and spin. In all three cases, the direction of travel is along the axis of the body. Microthrusters are placed around the perimeter of the cylindrical body and the thrust directions are outward from the body in the maneuver plane. Fin- and gyro-stabilized vehicles have negligible rotation, ω, about the travel axis. In these cases, impulses are simply applied in an appropriate direction for maneuvering. Spin-stabilized vehicles are much more challenging for impulse control because the orientation of the microthruster rotates in the maneuver plane. This places stringent timing requirements on the onset and duration of each microthruster impulse. In addition, control systems are required to track the angular position of the vehicle in order to apply impulses in the appropriate direction. For reference, a 60 Hz spin rate with 4 steering directions requires 4.16 ms control of the microthruster. High spin rates require even greater timing control of the microthruster. With appropriate timing, microthrusters can be used for maneuvers in these spinning systems.

A particular application of interest is the control of short-flight, spin-stabilized bodies. The vehicle for this investigation had a spin

* Corresponding author. Tel.: +1 404 913 6367.
E-mail addresses: anglaise@bellsouth.net, brian.english@engeniusmicro.com (B.A. English).

0924-4247/$ – see front matter © 2011 Elsevier B.V. All rights reserved.
doi:10.1016/j.sna.2011.09.017

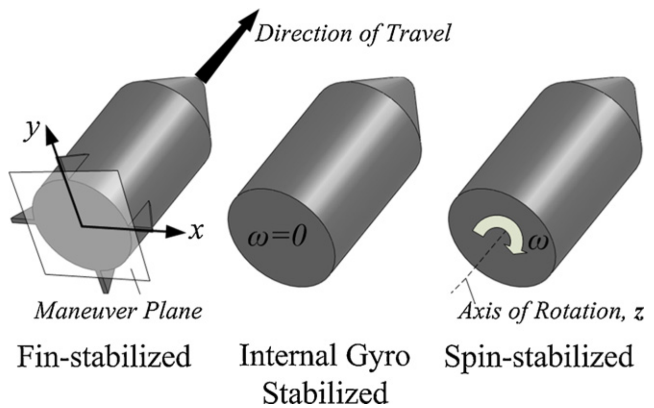

Fig. 1. Control surfaces that act in the maneuver plane must account for body rotation.

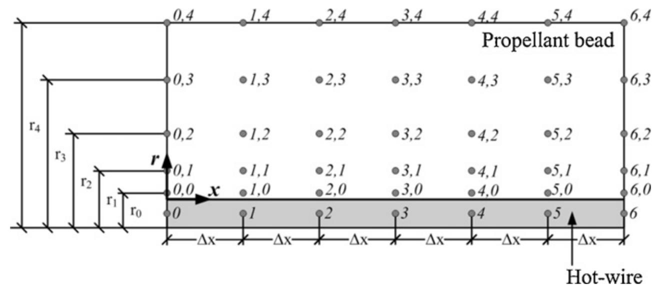

Fig. 2. Finite-difference heat-transfer model of hot wire and propellant.

rate of 60 Hz and flight time of less than 10 s. Also, vehicle payload constrained constrained the microthruster array and power supply to 30 mm long by 14 mm in radius and less than 100 g (10% of the flight vehicle weight). The ignition system design of microthrusters in these vehicles influences critical performance parameters, such as ignition delay, ignition delay variation, initiator energy consumption, power supply volume, and power supply weight. The ignition delay and delay variation determines how reliably the combustion force will begin on time. The igniter energy consumption affects the power supply design and volume.

Previous microthrusters igniters have been demonstrated with deposited metal [6,8] and polysilicon bridges [4,5,7], having resistances on the order of 100s or 1000s of Ohms, respectively. These ignition systems were well-suited for their missions, but did not require precise control of the ignition timing. For example, polysilicon bridges with a 50 μs ignition delay required a 100 V, 47 W power supply [1]. Depending on the required actuation rate, a power supply at this voltage could become impractical for sub-kg vehicles due to weight and volume constraints. Polysilicon igniters requiring smaller power supplies (80–150 mW) were demonstrated but ignition delays ranged between 17 and 750 ms [2]. Moreover, the ignition delays for these devices varied by at least 50 ms. Many of these previous microthruster igniters, while ideal for microsatellite applications, were limited to non-spinning bodies where precise timing was not critical. Other ignition systems which use laminated metal foil demonstrated reduced voltages and significantly reduced ignition delays [9,10]. These systems utilized 8 and 12 V supplies (2 and 3 cell 200 mAh lithium polymer batteries) and achieved mean ignition delays as low as 1 ms, ranging between 0.65 and 2.62 ms.

The presented work studied thermal interactions between laminated, metal-foil, hot-wire igniters and exothermic solid-state, composite chemical systems in order to demonstrate precise timing control of a thermal ignition process. The chemical system used was a composite propellant consisting of 25–45 radius oxidizer particles in a urethane binder and heating times were on the order of 1 ms.

The thermal interaction study of the laminated metal film igniter included analysis, fabrication, and characterization. The analysis included both a finite difference analysis and a finite element analysis. The finite difference analysis referenced a US Navy report that studied ignition times for nichrome wire igniters with constant current power supplies. This report demonstrated less than 3% error between the finite difference model and extensive testing [11], but does not explain why the chemical reaction is negligible. This analysis was modified for battery supplies assuming a constant voltage with an effective series resistance. Then, a finite element model was developed for the same assumptions as the reference simulation. The fabrication process included lamination, laser patterning, and photolithography to fabricate igniters and microthrusters. The fabrication enabled the use of the microthrusters in high-shock applications, and the microthrusters were demonstrated in a gun-launched, spin-stabilized flight system with an initial setback acceleration of 10,000 g [9]. The characterization of the ignition process includes voltage and current measurements for the metal-foil igniter of the microthrusters. The experimental results were compared with transient electrothermal models to determine sources of variation in the hot-wire system.

2. Modeling

Ignition is an initial, transient period of a combustion process that begins with the application of a stimulus, such as heat, impact, or friction, and ends when the combustion process is self-sustaining. The ignition system should initiate combustion in a controlled, predictable manner, and ignition is successful when combustion continues after the removal of the initial stimulus. The modeling presented focused on the interaction between the power supply and the laminated metal-foil igniters to achieve ignition. For a given propellant, the ignition system affected the following performance variables: ignition delay, ignition delay variation, ignition energy, and pulse power. The control variables in the electrical system included the igniter geometry, power supply voltage, and the power supply internal resistance. The ignition model was used to determine design points for the hot-wire geometry and to determine how these variables facilitated minimizing the weight and volume of the power supply.

2.1. Simulation setup

A voltage source model of the igniter, power supply, and fuel bead was developed based on an existing current-source model (NWL1919) [11]. NWL1919 is an implicit-step, finite-difference conduction model that demonstrated less than 3% error compared to extensive characterization using 45-μm radius, 2.85-mm long nichrome hot-wires and 0.4-mm radius potassium perchlorate/zinc propellant beads. This previous work was similar to the microthruster in terms of size and propellant chemistry, so it was chosen as a suitable modeling reference. The voltage-source model presented increased the number of discrete points to allow increased propellant thickness and increased igniter lengths compared to the NWL1919 model. Also, the electrical modeling was adapted to represent a constant voltage battery supply with a finite internal resistance.

Fig. 2 represents the numerical model used to estimate the propellant temperature, $T_f(x,r,t)$, during ignition. The model assumed the system was axisymmetric around the x-axis and symmetrical across the r-axis. Ambient temperature, T_a, was assumed uniform and constant at points where $x = 6$ and where $y = 4$. Thermal transfer in the x direction at points where $x = 0$ were assumed to be

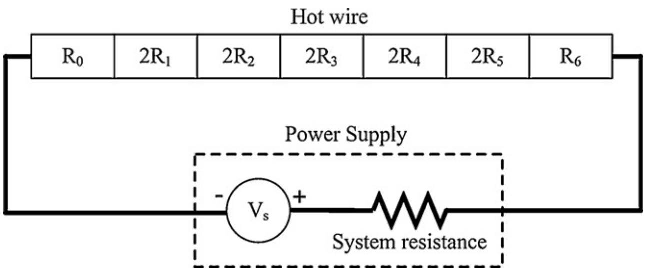

Fig. 3. Finite-difference electrical model of hot wire.

negligible due to symmetry. Heat generation was assumed to be negligible before ignition. Finally, the thermal diffusivity of the propellant, α_f, was assumed to be constant. With these assumptions, the temperature in the propellant normalized to the ambient temperature, $\theta_f = (T_f - T_a)$, was:

$$\frac{\partial \theta_f}{\partial t} = \alpha_f \nabla^2 \theta_f$$

In order to couple the thermal system with the electrical input system, the hot-wire temperature was modeled as a series of resistive heating elements with, as shown in Fig. 3. The resistance of each igniter element, R_i, was calculated for the local temperature, T_i, at each time step using the following equation:

$$R_i = \frac{\lambda_0 (1 + \mathrm{TCR} \cdot T_i)}{A_{ig}}$$

where λ_0 is the resistivity of the hot-wire at 25 °C, TCR is the thermal coefficient of resistivity, and A_{ig} is the cross-sectional area of the hot-wire.

Accurate accounting of total resistance, R_{tot}, was important because the igniter resistance was on the order of 1 Ω. The system resistance, R_{ps}, was measured and includes the internal resistance of the batteries, contact resistances, and line resistance, as seen in the following equation:

$$R_{tot} = R_{ps} + R_0 + 2\sum_{i=1} R_i$$

The open-circuit battery voltage was divided by this total resistance to yield the hot-wire current at each time step. This current was then substituted into the heat equation for the hot-wire. The heat equation included Joule heating (Term 3) and radial conduction (Term 4) from the igniter to the propellant, as seen in the following equation:

$$\frac{\partial \theta_{ig}}{\partial t} = \alpha_{ig} \nabla^2 \theta_{ig} + \frac{\iota^2 (1 + TCR \cdot \theta_{ig})}{\rho_{ig} A_{ig} c_{ig} \lambda_{ig}} - \frac{P_{ig} h}{\rho_{ig} A_{ig} c_{ig}} (\theta_{ig} - \theta_s)$$

where P_{ig} is the heated perimeter of the hot-wire, θ_s is the temperature of the propellant at the propellant-igniter interface, h is heat transfer coefficient at the interface, and other variables are defined in Table 1. The defined numerical model was used to determine hot-wire design points for spin-stabilized vehicles. The model was solved for a copper-nickel alloy (70 wt.% Cu) with properties listed in Table 1.

Table 1
Properties of 70/30 wt.% copper–nickel alloy hot wire [12].

Density, ρ_{ig}	8.913 g/cc
Specific heat, c_{ig}	400 J/kg-K
Resistivity, λ_{ig}	41.2 μΩ-cm
Thermal coeff. of resistivity, TCR	10^{-4} 1/K
Thermal conductivity	29.4 W/m-K
Melting temperature	1170 °C
Thickness	16.4 μm

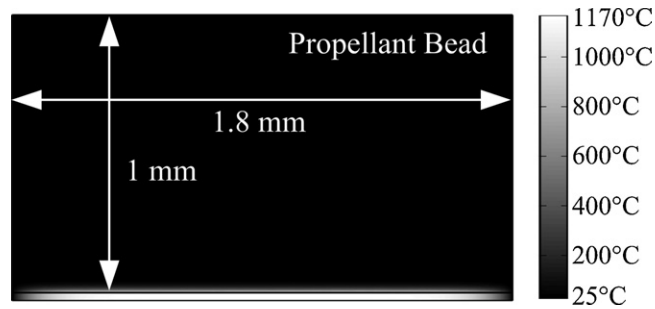

Fig. 4. FEA solution at 2.21 ms for 56-μm diameter, 1.8-mm long CuNi igniter.

CuNi was advantageous as a hot wire material because it heated rapidly due to a smaller heat capacity compared to other resistive heating metals. Propellant values of the convection coefficient (0.4368 W/cm²/K), specific heat (1.030 J/g K), propellant density (2.52 g/cc), and thermal conductivity (2.113 × 10^{-3} J/cm/K) were assumed to be equivalent to the reference model because the systems and propellant were similar. In addition to this model, a FEA analysis was of this system was solved where the fuel was in contact with the igniter wire with zero thermal contact resistance. This assumption eliminates the artificial use of the heat transfer coefficient, h, and reduces the analysis to a coupled transient conduction/Joule heating system. Both models were in agreement for the size scales of igniters tested, and these results will be discussed further in subsequent sections.

2.2. Simulation results

The laminated metal-foil igniter was heated when a voltage was applied. The voltage at any given time was dependent on the igniter resistance, which changed with temperature, and the internal resistance of the power supply. Fig. 4 represents the temperature profile in the propellant bead and the igniter when the metal foil began to melt at 1170 °C at 2.21 ms. This particular case, referred to as the “control case”, was a 1.8-mm long, 28-μm radius CuNi igniter with an 8.2 VDC, 1 Ω power supply. Fig. 4 shows that much of the propellant bead was unheated during the ignition process and the temperature in the igniter was uniform over much of its length. The temperature gradient at the wire–propellant interface corresponded to heating rates of 6.1 W, and the temperature gradient at the igniter wire ends represented heat loss rates of 1.6 W due to conduction out of the ends of the igniter. To illustrate the ignition process, Fig. 5 shows the temperature profile vs. time in the propellant. The red line represents when the hot-wire reached its

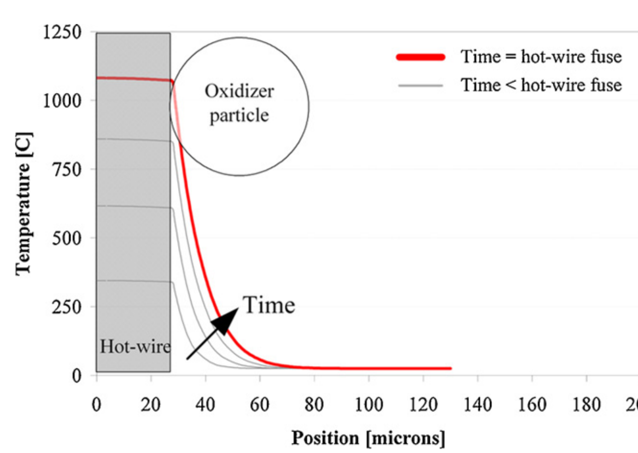

Fig. 5. Simulated temperature profile in hot-wire and propellant as time increases.

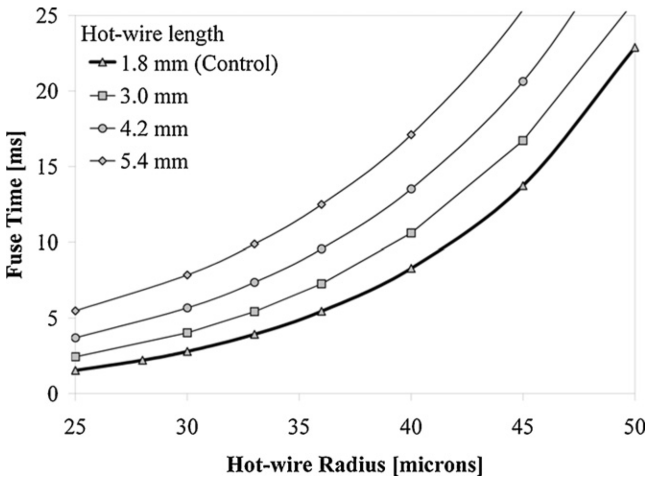

Fig. 6. Hot-wire design for 8.2 V, 1 Ω power supply.

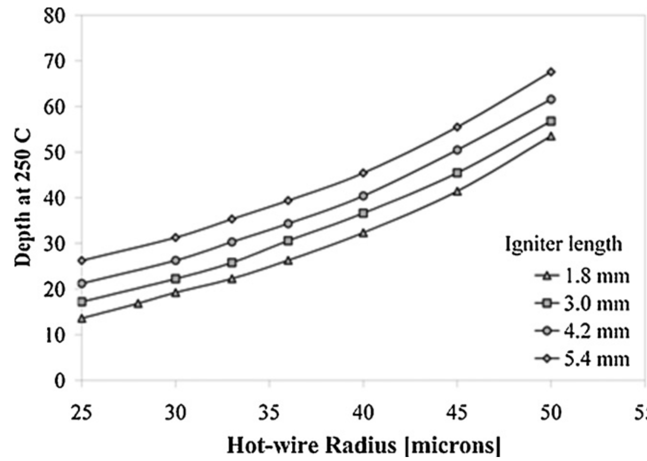

Fig. 7. Propellant depth (μm) where temperature is 250 °C.

melting temperature and electrical heating input ended. To show scale of the heating depth when the hot-wire melts, a hot-wire and an oxidizer particle were drawn on the plot. From the drawings on the plot, it is clear that the oxidizer salt was partially heated when ignition occurs. This small heated volume of propellant reacts, generates heat, and then propagates the reaction through the bulk of the propellant without additional heat input from the hot-wire. Optimization of the heat-transfer process at the hot-wire/propellant interface is dependent on the proximity of the oxidizer particles to the igniter surface and the geometry of the hot-wire. Efficient igniter design should then minimize the energy required from the power supply while generating sufficient chemical reactions to sustain the combustion of the propellant.

2.3. Metal-foil igniter design

The igniter design, i.e., length and width, was varied in the simulation to predict effects on the fuse delay and the heating depth. The fuse delay was important for determining control delays during microthruster actuation. The heating depth represents inefficiencies that could require larger power supplies. A solution set for this analysis is shown in Fig. 6 for an 8.2 VDC power supply with a 1 Ω internal resistance. With this power supply, 1.8-mm long hot-wires with radii of 25, 30, and 36-μm fused in 1.5, 2.8, and 5.5 ms, respectively. Also, 30-μm radius hot-wires with lengths of 1.8, 3.0, and 4.2 mm fused in 2.8, 4.0, and 5.7 ms, respectively. Reducing either the igniter radius or length reduced the fuse delay to milliseconds, and the size scales represented are well-suited to standard microfabrication or laser patterning techniques. Fig. 7 shows the distance where the propellant reaches 250 °C from the propellant–igniter interface, i.e., the heated depth above the ignition temperature, and higher values represent energy loss to unnecessarily heated propellant. The energy used to heat the extra propellant must be supplied by an incrementally larger power supply.

If short delays and efficient igniters were the only goal of igniter design, then this study would simply identify the shortest, thinnest igniter as the optimal choice. However, igniter design must account for the anticipated burn profile of the propellant. For example, in applications requiring a large initial flame front, an igniter with more area would be required. Two techniques to achieve a larger ignition area are to increase the radius or length of the igniter. The simulation showed that increasing the length of the igniter was preferable to increasing the radius because increasing the length minimized the ignition delay and minimized conductive heating losses into the propellant depth and out of the ends of the igniter.

2.4. Power supply design

Sensitivity analysis of the ignition delay vs. the power supply design was used to achieve controllable ignition delays with sub-100 g battery supplies. The power supply design, i.e., the open circuit voltage and equivalent series resistance (ESR), was varied to determine their effects on fuse delay. The weight and volume of a battery supply typically increases with increasing voltage and with decreasing ESR. The voltages simulated in Fig. 8 represents a two and three cell lithium–polymer battery pack. Increasing the voltage in the control case significantly reduced the fuse delay, especially as the igniter radius was increased. Also, as the battery voltage decreased during use, the fuse delay would increase. For example, at 8 V a 3% drop in voltage caused the ignition delay to increase 0.21 and 0.68 ms for the 28 and 35-μm radius igniters, respectively. In Fig. 9, 20% changes to the power supply ESR generated large changes in the igniter fuse delay. For example, a 20% increase in ESR increased the fuse delay 1ms and 3 ms for 28 and 36-μm radius igniters, respectively. Lowering the ESR is primarily accomplished with larger batteries or by connecting batteries in parallel; however, both solutions require that increased volume for the power supply. From Fig. 9, reducing the igniter width minimizes unacceptable fuse delay variation and maximizes volume savings in the power supply. The power supply study suggests that increasing power output improves control of the fuse delay variation. However, this has limited use in many applications because the power

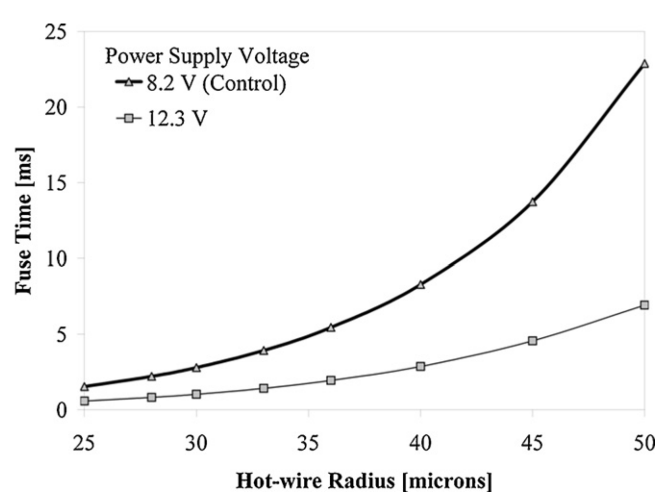

Fig. 8. Fuse delay vs. 1 Ω power supply voltage for 1.8-mm long igniters.

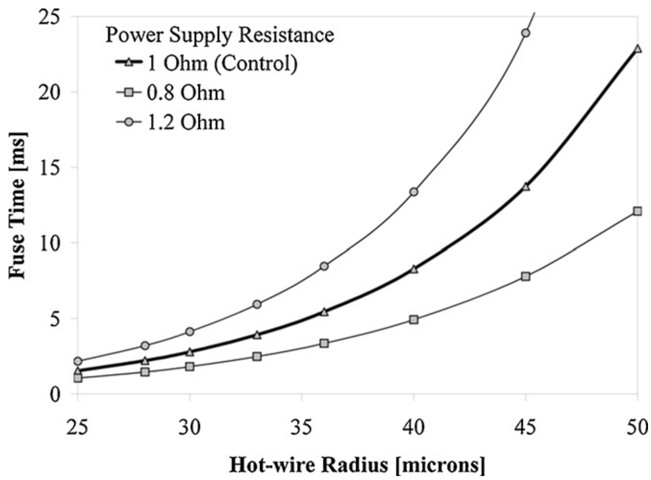

Fig. 9. Fuse delay vs. 8.2 V power supply resistance for 1.8-mm long igniters.

supply volume and weight will increase with power output, and volume must be balanced with control needs.

2.5. Ignition delay variation

Finally, sensitivity analysis of ignition delay vs. processing and system variations were further explored to determine which design variables should be controlled to minimize variations in the ignition delay.

To study the effects of processing and system variations in detail, a polynomial fit of the numerical results was calculated and then differentiated with respect to the input variables. This analysis of ignition delay variation versus variations in igniter radius, igniter length, system resistance, and power supply voltage are shown in Fig. 10. This analysis was solved for input perturbations to a system where the igniter length was 3 mm, the supply voltage was 8 V, the system resistance was 1 Ω, and the igniter radius was 27.4 or 35.3 μm. The variations listed in the caption were observed standard deviations. As seen in Fig. 10 the system resistance and hot-wire width had the greatest effect on the input variation for the design points evaluated. These effects were mitigated by decreasing the igniter width or better controlling the igniter width. From these results, the ignition delay variation was best controlled by minimizing the igniter width and establishing secure electrical connections. Efforts to increase the power supply were less desirable because they could lead to larger electrical components.

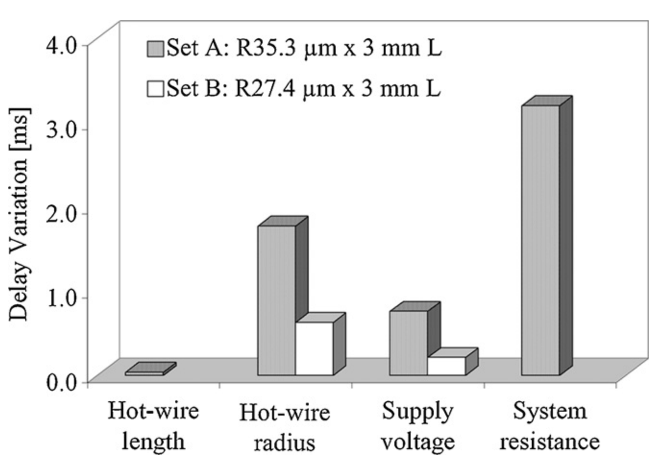

Fig. 10. Fuse delay sensitivity to processing and supply variations. Length (3 ± 20 μm), width (±20 μm), supply voltage (8 ± 0.25 V), system resistance (1 ± 0.2 Ω).

3. Fabrication

The fabrication process included propellant processing, actuator fabrication, and actuator array assembly. Beginning with the propellant, $KClO_4$ and $K_3Fe(CN)_6$ were first dried in a Shel-Lab vacuum oven at 200 °C for 12 h. Then the powders were ground in separate 28.5 mm radius ball mill at 120 rpm using 1/2 in. ceramic, cylindrical grinding media. Powders were then separately sorted using stacked sieves and a motorized shaker. Sieve sizes were 500, 212, 90 and 53 μm; 53–90 μm powders were used to fill the microthrusters. After sorting, powders were again dried for 12 h at 200 °C. Next, powders were manually mixed in 2 g batches. The propellant was diluted with acetone to facilitate loading of the composite propellant with a 0.419-mm radius syringe. The loaded actuators were then cured for 12 h at room temperature at 7% relative humidity. The propellant was finally sealed within the combustion chamber.

The actuator fabrication was based on printed circuit board (PCB) fabrication techniques. The fabrication process is shown in Fig. 11. Actuator fabrication began with patterning of backing and chamber layers of cured epoxy core (Isola FR406), Fig. 11a. FR406 was patterned by conventional machining. 16.4-μm thick metal foil (HPMetals CuNi715) was bonded to the base layer with uncured, low-flow, prepreg epoxy (Isola FR406). The igniter layer was patterned using photoresist and a wet FeCl etch. The combustion chamber was then bonded to the igniter and substrate, Fig. 11c, using uncured, low-flow, prepreg epoxy (Isola FR406). Next, Fig. 11d, composite propellant ($KClO_4/K_3Fe(CN)_6$/nitrocellulose laquer) was thinned using acetone and piped by syringe into the combustion chambers. The bonding surfaces were manually cleaned with acetone and methanol. Finally, Fig. 11e, layers of prepreg and epoxy core were laminated to seal the combustion chamber.

Fabrication processing results are shown in Fig. 12. The microthruster design was panelized into 24 disks of eight 17.2 mm^3 microthrusters. The upper volume of the propellant is limited by the need to exhaust the generated gas quickly. The number of microthrusters within the array is limited by the need to individually address each device. Propellant was diluted with acetone to reduce the viscosity, loaded into the combustion chamber, and allowed to dry. Propellant that filled the nozzles was cleaned with a razor blade after drying. The combustion chambers shown were 0.69-mm thick with a nozzle throat area of 0.70 mm^2. The nozzle divergence angle was 17°. The image of the panelized arrays shows the process after propellant filling. The microthruster disk in Fig. 12 (right) shows the completed fabrication with the microthrusters soldered to a PCB connector substrate.

After fabrication, the microthrusters were detached from the panel and mounted to connector boards. The final fabrication, Fig. 13, shows a stack of 4, 15-mm radius, microthruster disks. The microthruster stack was 6-mm tall, and the connector board was sized to enable a compression fit within the final flight vehicle. MOSFETs were embedded within cutouts in the microthruster disk to facilitated addressing of the 32 microthrusters. Power and signal pathways were soldered, providing electrical connectivity and also connecting microthruster disks to one another. These devices were completely finished and ready to be loaded into the flight vehicle. Microthruster fabrication demonstrated mass manufacture of microthruster arrays using PCB technology and assembly of microthruster arrays using common soldering techniques.

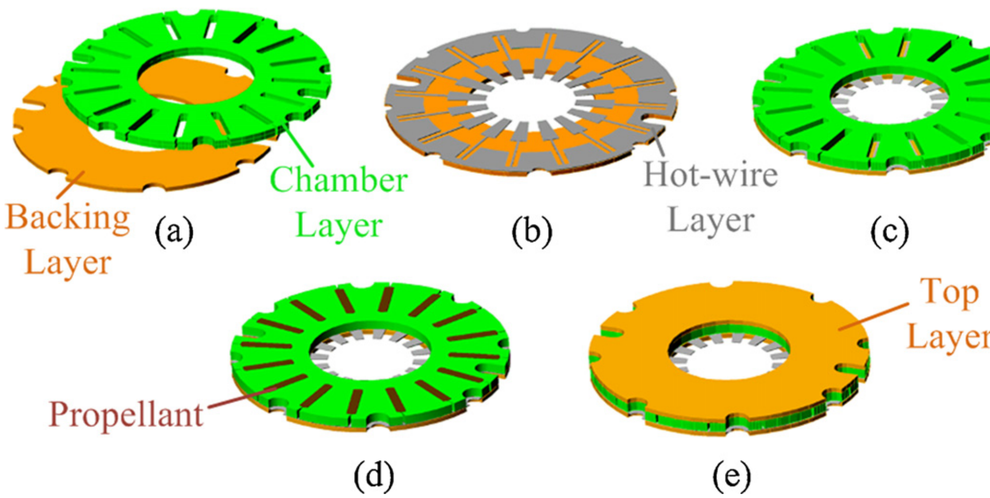

Fig. 11. Fabrication process for radial-thruster, laminated microthruster array.

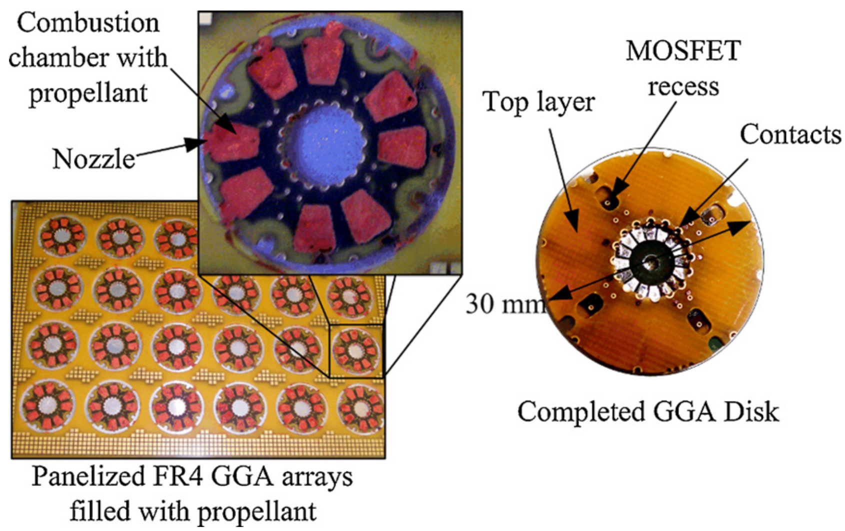

Fig. 12. Image of microthrusters after propellant filling and image of completed fabrication of single 30-mm diameter microthruster disk.

4. Characterization

The microthrusters were characterized to determine the actual fuse delay and ignition energies with respect to the design space predicted by the simulation.

4.1. Experimental setup

The circuit shown in Fig. 14 is used to characterize the hot-wire effects on the ignition delay and ignition delay variation. The batteries (Ultralife 641730, 200 mAh lithium polymer) charged a

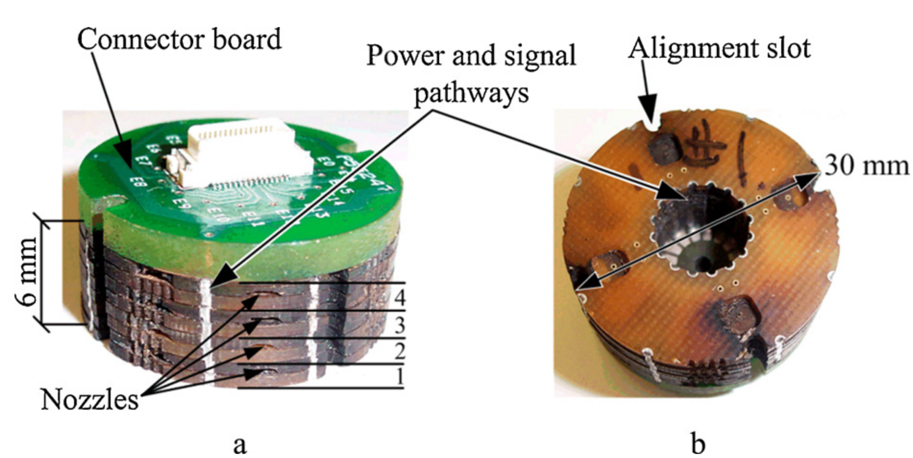

Fig. 13. Completed assembly and fabrication, (a) top view and (b) bottom view.

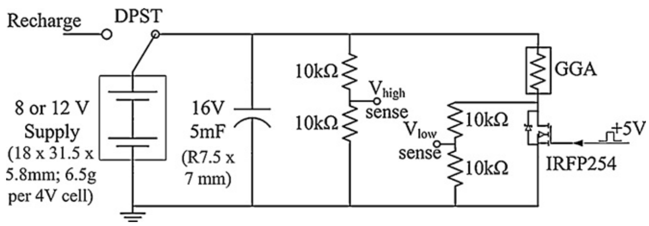

Fig. 14. Ignition characterization circuit.

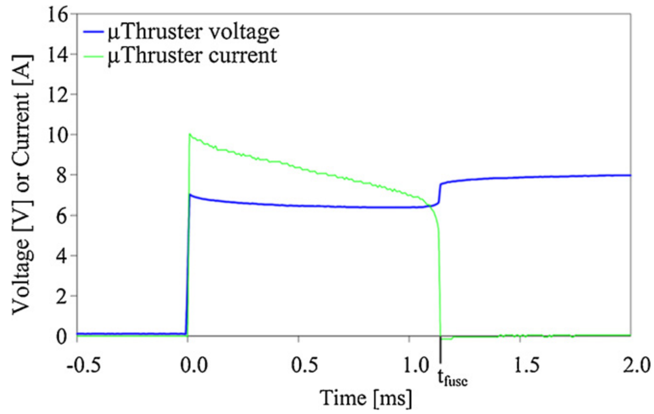

Fig. 15. Electrical measurements for 150-μm wide, 3-mm long, CuNi715 hot-wire.

capacitor (Evanscap THQA2) and powered the microthruster. A 5 volt input from a pulse generator to the gate of a power MOSFET (International Rectifier IRFP254, Max ratings: 250 V, 23 A), closed the circuit. Voltage was sampled at 120 kHz using a DAQ-board (National Instruments MIO-16E), a BNC break-out box (National Instruments 2090), an AMD 433 MHz PC, and Labview 6.0. The voltage measurements were taken at positions immediately before and after the combustor using the voltage divider circuits shown.

A sample electrical trace is presented in Fig. 15 for a 2-cell power supply and a 150-μm wide by 3-mm long CuNi715 hot-wire. The microthruster voltage was calculated by doubling the measured voltage difference between V_{high} and V_{low}. The microthruster current was calculated by doubling the measured voltage at V_{low} and then dividing by the 0.1 Ω on-resistance of the MOSFET. This constant resistance was assumed because drain-source voltage was fully in the linear regime of the MOSFET performance curve. Expectedly, the microthruster voltage and current decreased as the capacitor drains, Fig. 15. The current decreased more rapidly than the voltage as the igniter metal resistivity increased with temperature. With respect to ignition, the igniter ceased to conduct (i.e., it fuses) at 1.3 ms, ending the electrical input to the ignition system.

4.2. Experimental results

The characterization of the igniter and power supply was completed for several igniter geometries. The igniters were patterned

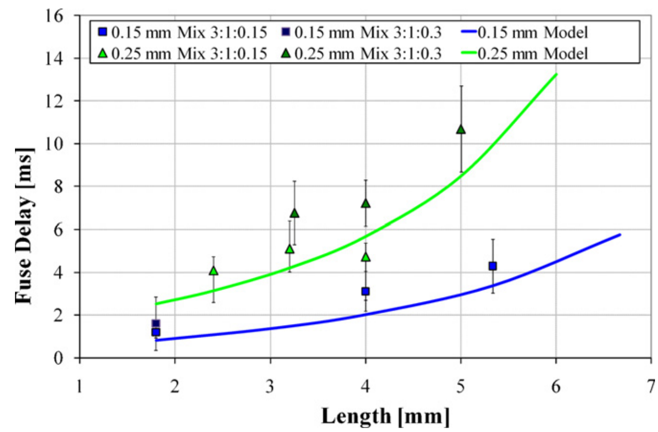

Fig. 16. Experimental results for CuNi715 igniters with 8.3 V 0.8 Ω power supply.

from 16.4-μm thick CuNi foil. The rectangular wires were compared to the circular models by equating the cross-sectional area of the igniters. Fig. 16 shows the characterization results for 0.15 and 0.25-mm wide igniters of varying lengths. The fuse delay variation was assumed to behave with a lognormal distribution to avoid distributions with negative fuse delays. The marker positions in Fig. 16 represent the lognormal mean of the igniter fuse delays, and the error bars represent 2σ variation of the natural log for each set of data points. As presented in this figure, each marker represents only one propellant composition, so the propellant formulation is not the same within each series. It was possible that varying the fuel formulation altered the heat transfer rate between the wire and the fuel, but the heat transfer coefficient was assumed constant because same nitrocellulose binder was used for all trials.

The first series of experiments compares igniters of varying length and width for a single power supply. The data showed that increasing either the igniter width or length increased the ignition delay. These experimental results were compared with the ignition model for an 8.2 V, 0.8 Ω battery supply. The finite difference model under-predicts the mean fuse time in all cases, e.g., by 0.5 ms for the 0.15-mm series. The difference between the model and the results can be attributed to two reasons. First, the battery voltage varied with time between 8.3 and 8.0 V, so the reduced voltage would cause an increased fuse time as seen in Fig. 8. Second, the actual power supply resistance was estimated based on resistance measurements across the microthruster assembly and technical data for the battery. As seen in Fig. 9, errors in the power supply resistance input to the model would lead to fuse time predictions that were shorter than observed. With respect to ignition delay variation, the fuse delay variation was less than 2 ms for all cases in the 0.15-mm series, and the 0.25-mm model variation ranged from ±1 ms to ±2.2 ms. This supported the modeling conclusion that thinner igniters enable better control of the ignition timing.

Finally, the experiments compared the performance of a single hot-wire geometry for a two and three-cell power supply with a single propellant formulations. The igniter was the 150-μm wide, 16.4-μm thick, 1.8-mm long CuNi715. The power supply was a two

Table 2
Lognormal fuse delay distribution of final CuNi715 hot-wire design. Igniter dimensions were 150-μm wide, 1.8-mm long.

	Two-cell supply			Three-cell supply		
	Δt_{fuse} (ms)	E_{ign} (mJ)	Trials	Δt_{fuse} (ms)	E_{ign} (mJ)	Trials
Max: $\exp(\overline{Ln(X)} + 2\sigma_{Ln(X)})$	2.62	125		0.84	127	
Mean: $\exp(\overline{Ln(X)})$	1.30	99	50	0.55	88	72
Min: $\exp(\overline{Ln(X)} - 2\sigma_{Ln(X)})$	0.65	78		0.36	62	

or three-cell supply consisting of 200 mAh lithium polymer batteries and a 5 mF capacitor. The results of this experiment, Table 2, showed that the two-cell supply could be used to control the ignition delay to within 1.97 ms (Max − Min), with a mean delay of 1.3 ms. The estimated fuse delay for the 8.2 V, 0.8 Ω power supply was 1.46 ms. By comparison, the larger three-cell supply reduced the ignition delay 57% to 0.55 ms and controlled the hot-wire fuse time to within 0.48 ms. The estimated fuse delay for the 12.3 V, 0.8 Ω power supply was 0.56 ms. Increasing the power supply also reduced the fuse energy by 11% from 99 to 88 mJ by reducing the heat loss to non-reacting regions of solid propellant. This is a small reduction in ignition energy, so increasing the power supply should be reserved for applications requiring greater ignition delay control rather than applications requiring less energy.

5. Conclusions

The study of the laminated metal-foil igniter demonstrated design simulations, fabrication techniques, and experimental evidence to control of ignition timing for microthrusters. The microthruster ignition was controllable to within 0.50 ms using a low-volume, low-voltage battery supplies. Also, ignition timing variation was minimized through control of the power supply lead resistance and through control of the hot-wire width. Accurate and precise timing as well as low volume power supplies are necessary to extend the use of existing microthrusters into spin-stabilized, sub-kilogram flight systems. The experimental devices were fabricated using inexpensive printed-circuit board fabrication, leveraging low-cost manufacturing and batch fabrication. This would be useful for non-consumer applications, where comparatively low-volume fabrication is needed for custom control systems. The fabrication and timing study together demonstrates that microthrusters are suitable for flight systems with spin-rates of 120 Hz using a two-cell 200 mAh lithium polymer supply and 500 Hz using a three-cell 200 mAh lithium polymer supply.

Acknowledgements

Thanks to the DARPA Micro-Adaptive Flow Control Program for funding. Thanks to Andre Lovas at Georgia Tech Research Institute for PCB fabrication support.

References

[1] A.P. London, A.H. Epstein, J.L.J.L. Kerrebrock, High pressure bipropellant microrocket engine, Journal of Propulsion and Power 17 (July–August (4)) (2001) 780–787.
[2] L. Garrigues, I.D. Boyd, J.P. Boeuf, Computation of hall thruster performance, in: IEPC-99-098, International Electric Propulsion Conference, Kitakyushu, Japan, October, 1999.
[3] D.T. Schappell, E. Scarduffa, P. Smith, N. Solway, Advances in marotta electric and small satellite propulsion fluid control activities, in: 41st AIAA/ASME/SAE/ASEE Joint Propulsion Conference & Exhibit, Tucson, Arizona, July, 2005 (AIAA 2005-4055).
[4] D.H. Lewis, S.W. Janson, R.B. Cohen, E.K. Antonsson, Digital micropropulsion, Sensors and Actuators A 80 (2000) 143–154.
[5] C. Rossi, D. Briand, M. Dumonteuil, T. Camps, P.-Q. Pham, N.F.d. Rooij, Matrix of 10 × 10 addressed solid propellant microthrusters: Review of the technologies, Sensors and Actuators A 126 (2006) 241–252.
[6] K.L. Zhang, S.K. Chou, S.S. Ang, Development of a solid propellant microthruster with chamber and nozzle etched on a wafer surface, Journal of Micromechanics and Microengineering 14 (2004) 260–266.
[7] D. Teasdale, Solid propellant microrockets, Masters Thesis, University of California at Berkeley, 2000.
[8] K. Zhang, S.K. Chou, S.S. Ang, Investigation on the ignition of a MEMS solid propellant microthruster before propellant combustion, Journal of Micromechanics and Microengineering 17 (2007) 322–332.
[9] B.A. English, Laminated Gas Generator Actuator Arrays, Ph.D. Thesis, Georgia Institute of Technology, 2006.
[10] B.A. English, P. Gadiraju, C.S. Rinehart, A. Glezer, M.G. Allen, Gas generator actuator arrays for flight control of spinning-body projectiles, Istanbul, Turkey, MEMS, Technical Digest (2006) 733–737.
[11] J.J. Massey, in: NWLD (Ed.), A Heat Transfer Model Study of the Hot Wire Initiator, National Technical Information Service, VA, 1964.
[12] H.P. Metals, Technical Data Sheet – CuNi715, 2006.

Biographies

Brian English is a Principal Investigator at EngeniusMicro, LLC in Atlanta, GA. He obtained his B.S. and M.S. of Mechanical Engineering in 1997 and 2011, respectively. He obtained his Ph.D. in 2006 for research developing laminated microactuators for flow control. He is currently pursuing Small Business Innovation Research through Federal Funding to commercialize emerging technologies. Research areas of interest include microfabrication, electronic packaging, active cooling,and wireless sensing.

Mark G. Allen received the B.A. degree in Chemistry, the B.S.E. degree in Chemical Engineering, and the B.S.E. degree in Electrical Engineering from the University of Pennsylvania, and the S.M. and Ph.D. (1989) from the Massachusetts Institute of Technology. In 1989 he joined the faculty of the School of Electrical and Computer Engineering of the Georgia Institute of Technology, where he currently holds the rank of Regents' Professor and the J.M. Pettit Professorship in Microelectronics, as well as a joint appointment in the School of Chemical and Biomolecular Engineering. His research interests are in the development and application of new micro- and nanofabrication technologies, as well as microelectromechanical systems (MEMS). He is Editor-in-Chief of the Journal of Micromechanics and Microengineering, previous co-chair of the IEEE/ASME MEMS Conference, and a Fellow of the IEEE.